

Observed flux density enhancement at submillimeter wavelengths during an X-class flare

G. Cristiani^{a,*}, C.G. Giménez de Castro^b, M.L. Luoni^a,
C.H. Mandrini^{a,1}, M.G. Rovira^{a,1}, P. Kaufmann^{b,c},
M. Machado^d

^a*Instituto de Astronomía y Física del Espacio, CC. 67 Suc. 28, CONICET-UBA, 1428, Buenos Aires, Argentina.*

^b*Centro de Rádio Astronomia e Astrofísica Mackenzie, Universidade Presbiteriana Mackenzie, São Paulo, Brazil.*

^c*CCS, Universidade Estadual de Campinas, Campinas, Brazil.*

^d*Comisión Nacional de Actividades Espaciales, Paseo Colón 751, 1063, Buenos Aires, Argentina.*

Abstract

We analyse the 30 October, 2004, X1.2/SF solar event that occurred in AR 10691 (N13 W18) at around 11:44 UT. Observations at 212 and 405 GHz of the Solar Submillimeter Telescope (SST), with high time resolution (5 ms), show an intense impulsive burst followed by a long-lasting thermal phase. EUV images from the Extreme Ultraviolet Imaging Telescope (SOHO/EIT) are used to identify the possible emitting sources. Data from the Radio Solar Telescope Network (RSTN) complement our spectral observations below 15 GHz. During the impulsive phase the turnover frequency is above 15.4 GHz. The long-lasting phase is analysed in terms of thermal emission and compared with GOES observations. From the ratio between the two GOES soft X-ray bands, we derive the temperature and emission measure, which is used to estimate the free-free submillimeter flux density. Good temporal agreement is found between the estimated and observed profiles, however the former is larger than the latter.

Key words: Solar Physics, Radio microwave, Radio Submillimeter, Flares

PACS: 96.60.-j, 95.85.Bh, 95.85.Fm, 96.50.qe

* Corresponding author

Email address: gcrystiani@iafe.uba.ar (G. Cristiani).

¹ Member of the Carrera del Investigador Científico, CONICET, Argentina

1 Introduction

It is widely accepted that solar flares imply the release of large amounts of energy, which go mainly in the acceleration of particles: electrons and ions. The interaction of these particles with the medium, plasma and magnetic field, produces radiation by very different mechanisms, which is observed at Earth in a wide range of wavelengths. Of particular interest are electrons moving along the magnetic lines and producing gyrosynchrotron emission observed at microwaves and shorter wavelengths. Gyrosynchrotron emission of mildly relativistic electrons is distributed in a broad continuum at high harmonics of the fundamental frequency $\nu_B = eB/(2\pi m_e c)$, where e is the electron charge, B the magnetic field strength, m_e the electron mass at rest and c the speed of light. The maximum emission is centred around $\nu \simeq \nu_B \gamma^2$, with γ the electron Lorentz factor (Dulk, 1985). Taking $100 \leq B \leq 1000$ G, indicative values of γ are between 2 and 5 for a 10 GHz photon. Observationally, Kosugi et al. (1988) found that the highest correlation between centimetric wavelengths and hard X-rays (HXR) happens between 17 GHz and 80 keV; that is, electrons with energies ≤ 200 keV. Therefore, radio observations at shorter wavelengths offer new insights to understand processes that involve high energy electrons during solar flares, where current HXR detector technology does not provide enough sensitivity and/or signal to noise ratios to observe weak flares. Since 1999, the only submillimeter instrument dedicated to solar observation is the Solar Submillimeter Telescope (SST, see e.g., Kaufmann et al., 2001) operating at 212 and 405 GHz. From the theoretical arguments given above, > 4 MeV electrons should produce the synchrotron emission observed with SST.

In this work, we report the multiwavelength observations of the impulsive and gradual phases of an X-class flare that occurred on 30 October, 2004. In the following section we describe the instruments and data analysis. In Section 3, we analyse the impulsive phase of the flare; while in Section 4, we do the same for the gradual phase. Finally, we give our concluding remarks.

2 Observations and principal characteristics of the event

The SST (Kaufmann et al., 2001) is a radome enclosed 1.5 m single dish antenna with room temperature receivers in a focal array: 4 at 212 GHz and 2 at 405 GHz, with 5 ms time resolution. On 30 October, 2004, SST was tracking AR 10691 (N13 W18) with its beam 5. In Figure 1, we sketch the position of SST beams with crosses on a 195 Å EUV image of EIT (Delaboudiniere et al., 1995); the size of the crosses is equal to the HPBW. While beams 2, 3 and 4 (212 GHz) are round, beam 5 (405 GHz) has an elliptical shape, with minor

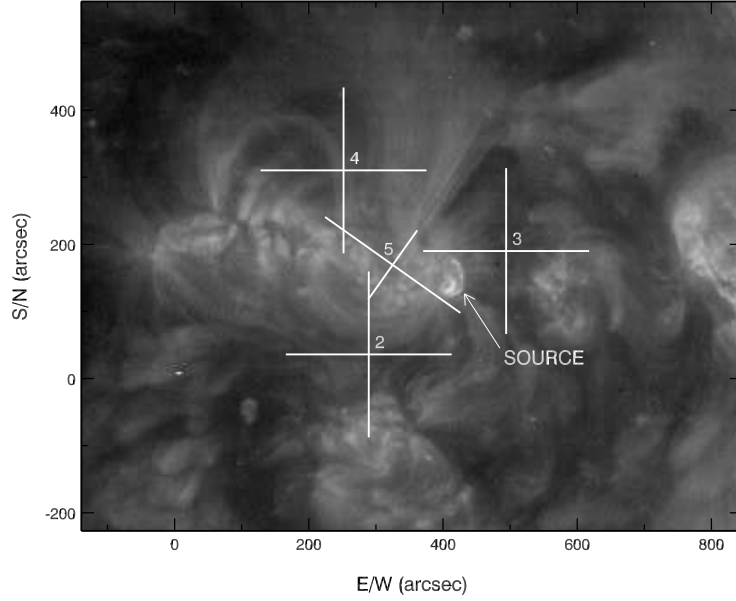


Fig. 1. A 195 \AA EIT image of the flaring area at 11:36:42 UT. North is up and east to left. The labelled crosses represent the SST beams: 2, 3 and 4 are 212 GHz receivers, while 5 is a 405 GHz receiver. Only beams 3 and 5 detected the burst.

and major axes in the directions shown in the figure. Because of the high atmospheric attenuation only two beams observed this event, one at 212 GHz (beam 3) and one at 405 GHz (beam 5). Beams 1 (212 GHz) and 6 (405 GHz) are not shown in the figure. Since only two beams observed the event, we cannot use the multibeam technique (Costa et al., 1995) to locate the centroid of emission.

Assuming that the radio source is coincident with the EUV bright loop (see Fig. 1), we correct the observed antenna temperature at 212 and 405 GHz for the misalignment. During calibration the antenna temperatures are also corrected for atmospheric attenuation. Finally, the corrected antenna temperatures are converted to flux densities, F , using the well known formula: $F = 2k_b T_a / A_e$, where k_b is the Boltzmann constant, T_a the corrected antenna temperature and A_e the effective area of the antenna. We estimate a 40% uncertainty for the whole process.

Data at microwave frequencies with 1 second time resolution were obtained by the Radio Solar Telescope Network (RSTN, Guidice et al., 1981). Figure 2 shows the time profiles of the event at different wavelengths. At 15.4 GHz, we see that the burst starts at 11:42:40 UT as a small enhancement that evolves into the impulsive phase with a maximum flux density around 3300 s.f.u. at 11:44:09 UT. The increasing phase is characterized by short emissions that can

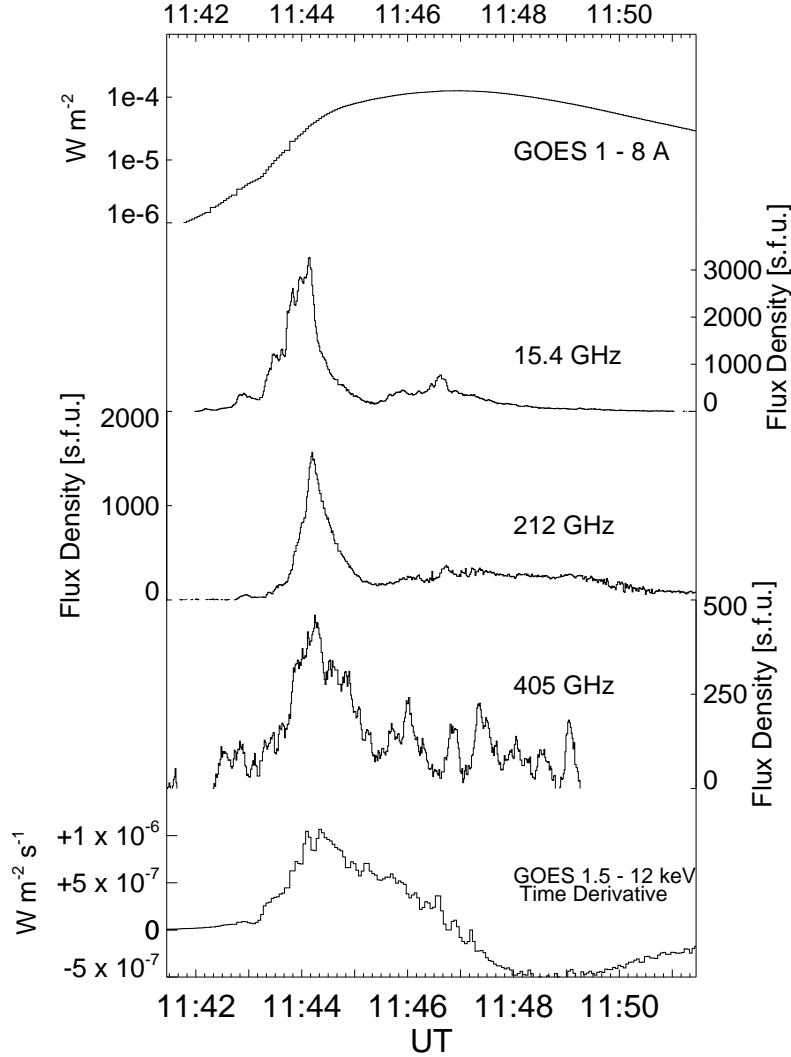


Fig. 2. Time profiles at selected wavelengths. GOES data have 3 seconds time resolution, radio data are integrated to 1 second.

be attributed to different particle injections. The decreasing phase is smooth, with no bursts, reaching the minimum value (close to the pre-flare level) at 11:45:25 UT. Afterward, a post burst increase is observed until approximately 11:51 UT. This gradual phase has also some bursting episodes characteristic of particle injections.

Although the 212 GHz time profile is in general smoother than that at 15.4 GHz, most of the features observed at 15.4 GHz are also present, with smaller amplitude, at 212 GHz. The starting time of the burst at 212 GHz coincides with that at 15.4 GHz (11:42:40 UT), but the peak time is delayed by 3 seconds (11:44:12 UT at 212 GHz). The gradual phase is also present with sudden changes, probably, of instrumental origin. The 405 GHz time profile

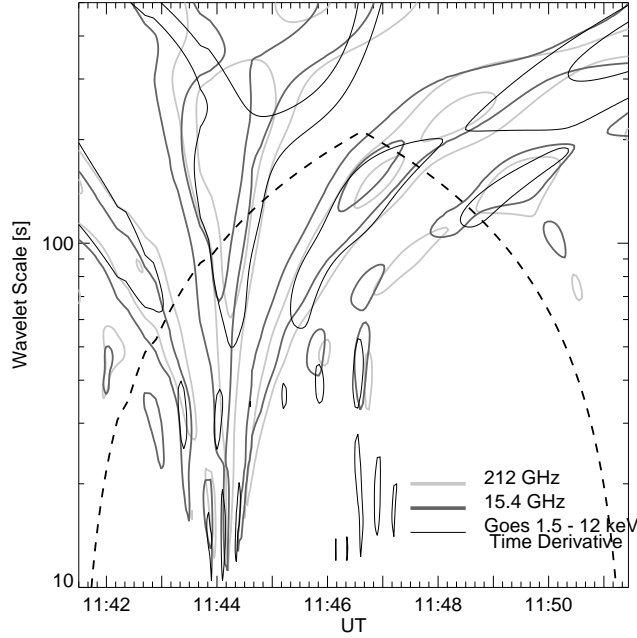


Fig. 3. Wavelet transform of the flux density at 15.4 and 212 GHz and GOES time derivative represented in a 2D graph. Contour levels are: 10^{-7} , 10^{-6} $\text{W m}^{-2} \text{s}^{-1}$ (GOES time derivative); 75, 750 s.f.u. (212 GHz) and 185, 1850 s.f.u. (15.4 GHz).

during the rising phase is closer to the 15.4 GHz emission than to the 212 GHz, is in general delayed in 6 seconds. The decaying phase is more extended than in the other frequencies and shows the presence of longer features, some of these features could have an atmospheric origin, and do not allow us to clearly recognize the gradual phase.

Unfortunately, no HXR data are available for this event. Instead, we have used the time derivative of GOES 1.5 – 12 keV soft X-ray (SXR) channel with 3 seconds temporal resolution to compare with the radio flux density. The sensitivity of GOES is better than $5 \cdot 10^{-8} \text{ W m}^{-2}$, taking this value as the flux uncertainty, the flux time derivative has a mean uncertainty better than $\sqrt{2} \cdot 5 \cdot 10^{-8} / 3 \text{ W m}^{-2} \text{ s}^{-1} \sim 3 \cdot 10^{-8} \text{ W m}^{-2} \text{ s}^{-1}$. The time derivative of GOES channel 3 (bottom curve in Fig. 2) mimics very well the radio time profiles during the rising phase and is coincident in time, but has two clear maxima, the first peaking in coincidence with the 15.4 GHz emission. We will show later that the second GOES time derivative peak, still during the rising phase, is also present at the other frequencies, but during their decaying phase. Finally, the decaying phase in this curve lasts longer than the others and has some bursting episodes.

We use the wavelet transform (see e.g. Daubechies, 1992) to compare the time profiles. Wavelets are very useful to discriminate the different time scales

in a time series. We have integrated our data to the lowest time resolution, namely 3 seconds and applied the wavelet transform implemented by Torrence and Compo (1998) based on a Morlet mother wavelet with wavenumber 6. In Figure 3 each contour represents a structure resolved by the transform with a characteristic scale in the ordinates occurring at the time in the abscissas. We note that for each frequency the minimum contour level plotted is much greater than the signal uncertainty. We have overplotted the density flux at 15.4 GHz (dark thick curve), 212 GHz (light thick curve) and the time derivative of the GOES flux (black thin curve). The dashed curve represents the *cone-of-influence* of the transformation, i.e., where the boundaries do not affect the result. We observe that near peak time (11:44 UT) there are three groups of structures with scales around 10–20 seconds. The first one, a little before 11:44 UT, is observed at the three frequencies with no appreciable delay between them. The second one, just after 11:44 UT is present also at the three frequencies. The last one ($\sim 11:44:30$ UT) is observed at 15.4 GHz and GOES time derivative. At 212 GHz, this structure appears only after 11:44:40 UT. Other structures with longer duration are also observed for the 40 seconds scale, around 11:45:50 UT and around 11:46:30 UT. In general, the wavelet transforms are similar for the different frequencies, including the coincidence in time of the characteristic features at the different scales. Time profiles do not reflect this in a more evident way because the relative importance of the pulses are different.

3 The impulsive phase

Figure 4 (left panel) depicts the time evolution of the 2.695 and 15.4 GHz emissions at the top, together with the temporal evolution of the optically thick spectral index at the bottom. This index is determined from the flux densities at 2.695, 4.995, 8.8 and 15.4 GHz. The index is lower than 1 all along the impulsive phase. The spectral index of the optically thick gyrosynchrotron spectrum originated in a homogeneous source is between 2.5 and 2.9 (Dulk, 1985), independently of the electron index. Therefore, our result is an indication of the presence of an inhomogeneous source.

The 40 ms integrated time evolution of the flux density at 212 and 405 GHz during the impulsive phase is shown in the right panel of Figure 4 (above). The bottom of this panel corresponds to the temporal evolution of the optically thin spectral index deduced from these flux densities, the only two frequencies that are optically thin in our data. During the central part of the impulsive phase (between the dashed lines in the right panel of the Fig. 4), the index is close to constant, with gradual transitions at the beginning and end. Therefore,

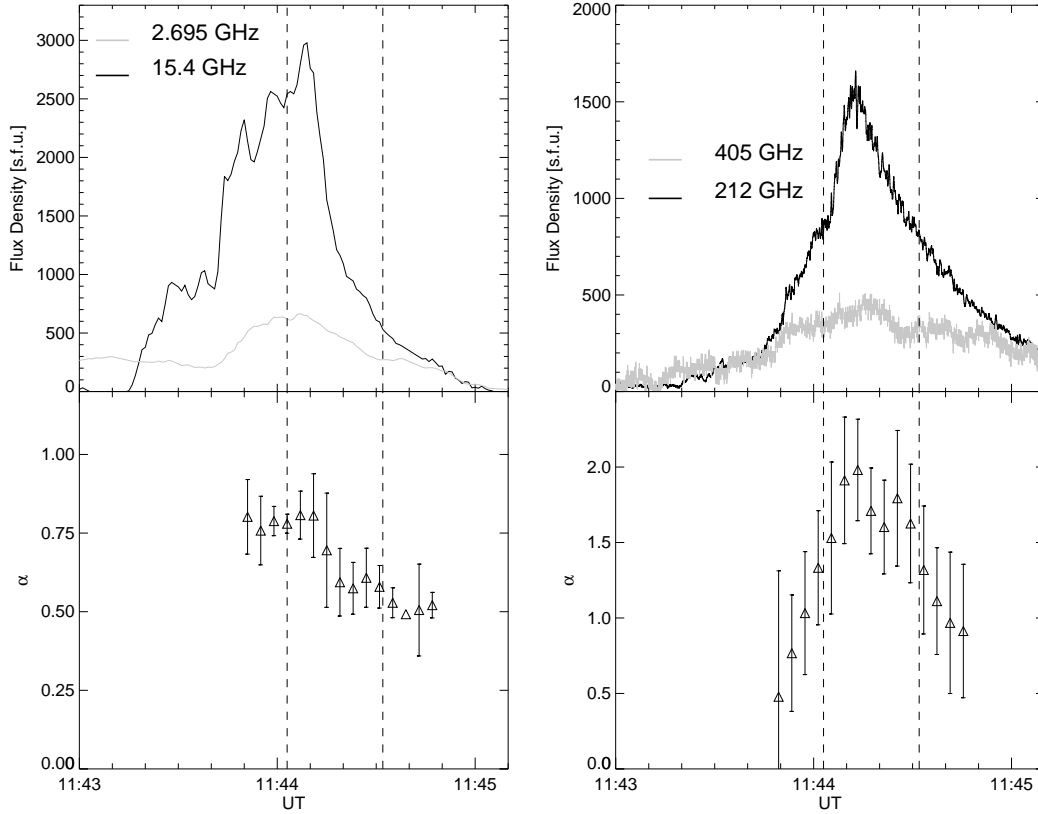


Fig. 4. Left panel: 1 s time profiles of 2.695 and 15.4 GHz flux densities from RSTN observations (above) and temporal evolution of the optically thick spectral index α obtained from the 2.695, 4.995, 8.8 and 15.4 GHz flux densities (below). Right panel: 40 ms time profiles of 405 and 212 GHz flux densities deduced from SST observations (above) and temporal evolution of the optically thin spectral index α obtained from the 405 and 212 GHz flux densities ratios (below).

we can characterize the peak time with only one electron population. Using Dulk’s formula (Dulk, 1985), we can estimate the electron energy index as $\delta \approx 3$.

The low spectral resolution of our radio data does not allow us to obtain a unique theoretical fit of the spectrum, i.e. different sets of parameters (magnetic field strength, viewing angle, source size, lower and higher cutoff energies, etc.) give similar results for the optically thin region; while, the optically thick region is never well fitted, as expected when an inhomogeneous source is present.

4 The 212 GHz gradual phase

The gradual phase is observed very clearly at 212 GHz (Fig. 5). At lower frequencies, after the main burst, new bursting episodes of gyroemission origin

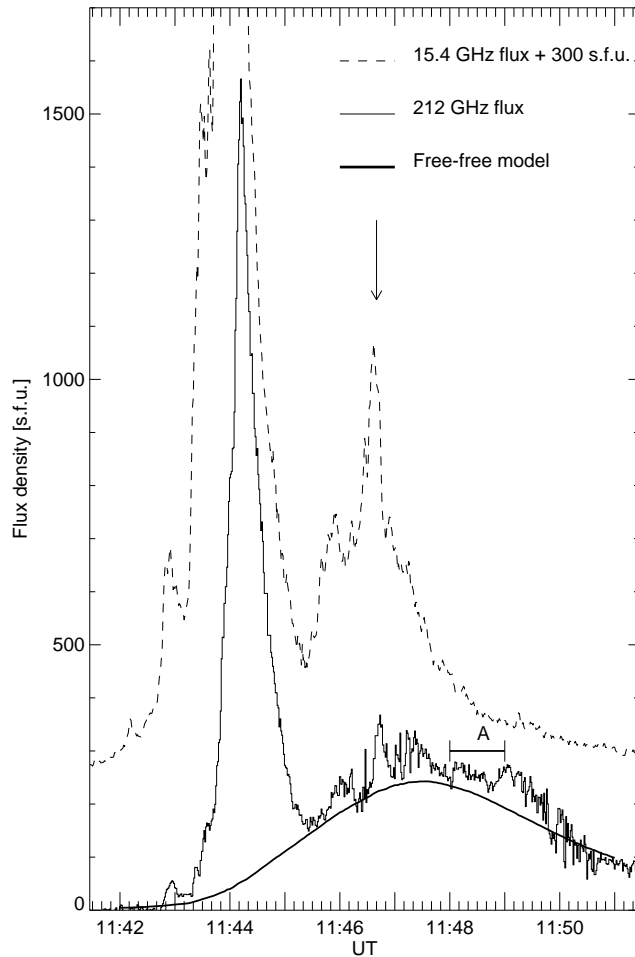


Fig. 5. The 212 GHz gradual phase. After the burst ($\sim 11:45:30$ UT), a gradual increase of the flux is observed at 212 GHz lasting until 11:51:30 UT. During the gradual phase, some bursting episodes are seen. In contrast, after 11:45:30 UT, the microwave flux, here represented by the shifted 15.4 GHz (dashed line), shows a second burst composed of many pulses. The most intense one is also observed at 212 GHz. Along interval **A** we integrate the flux density at the different frequencies to obtain one spectrum (Fig. 6). The continuous thick line represents the expected emission of a thermal bremsstrahlung.

are seen. Figure 5 shows the 15.4 GHz flux density, arbitrarily shifted by 300 s.f.u., to clarify the plot; the late bursting episodes are evident in this figure. The strongest 15.4 GHz feature is also observed at 212 GHz (arrow in Fig. 5). Variations in the atmospheric attenuation and/or emission are relatively more intense at 405 GHz than at 212 GHz, and thus they modulate the background making the free-free emission difficult to observe.

To test the thermal bremsstrahlung hypothesis we have modelled the observed emission as an isothermal homogeneous bremsstrahlung source. We integrate

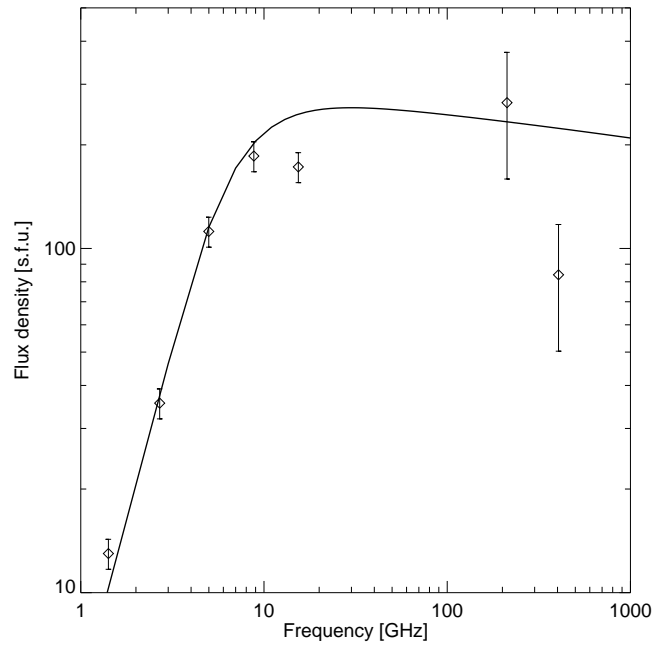


Fig. 6. Spectrum of the flux density during the interval 11:48 – 11:49 UT. The solid curve represents the expected emission of an isothermal bremsstrahlung source.

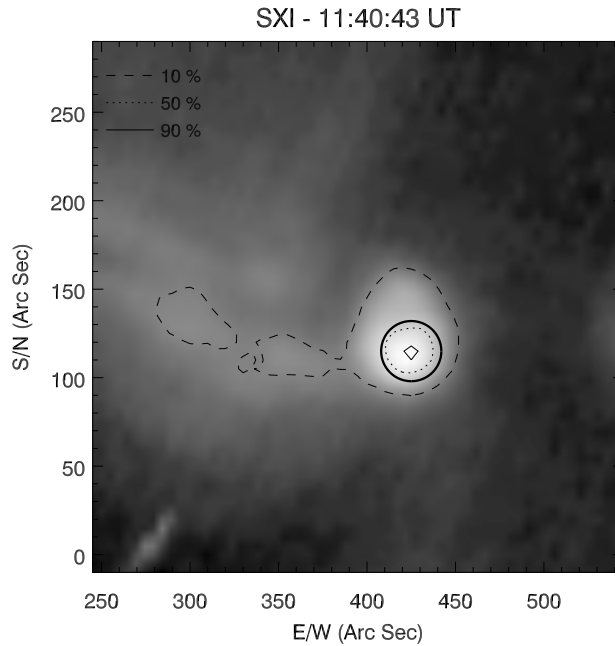


Fig. 7. A soft X-ray image taken by SXI of the flaring area just before the maximum of the flare. The contours represent the emission levels of the thermal source. The circle corresponds to the source of our isothermal bremsstrahlung model.

the flux densities at different frequencies in the 1 minute interval shown in Figure 5 with a label 'A' to obtain the gradual spectrum. We have not tried to subtract the contribution from other emission mechanisms, like gyrosynchrotron; therefore, we choose an interval that does not show strong gyroemission. To determine the size of the source we have used an image from the Solar X-ray Imager (GOES/SXI, Hill et al., 2005; Pizzo et al., 2005) (Fig. 7), considering the emitting area above 30% of the maximum, which yields a source size of the order of $40''$. The emission measure and temperature of the source are determined using the Chianti-based model with coronal abundances and the response of GOES detectors. We fit the expected emission to the observed data, having as free parameters the source size and the source depth and we include a multiplicative factor ζ . The time profile of the gradual emission at 212 GHz must be fitted simultaneously. We have obtained the best fit with a source size of $28''$, $8.4 \cdot 10^8$ cm depth and $\zeta = 7.5$. Figures 5 and 6 show the results. The temporal evolution of the model is remarkably similar to the gradual phase of the 212 GHz emission. Moreover, the modelled spectrum follows the observed one.

The homogeneous and isothermal thermal bremsstrahlung flux density, $F(\nu)$, is:

$$F(\nu) = \zeta \frac{2 k_B T \nu^2}{c^2} (1 - \exp(-\kappa_\nu H)) \Omega , \quad (1)$$

where κ_ν is the absorption coefficient, H is the depth of the source and Ω the source solid angle, while T represents the source temperature and ζ is our multiplicative factor. The absorption coefficient κ_ν can be approximated by (Dulk, 1985):

$$\kappa_\nu \simeq \frac{0.2 N_{med}^2}{T^{3/2} \nu^2} \text{ cm}^{-1} , \quad (2)$$

with N_{med} the thermal plasma density. In the optically thick regime, where $\tau_\nu = \kappa_\nu H \gg 1$, Eq. 1 tends to:

$$F(\nu) \simeq \zeta \frac{2 k_B T \nu^2}{c^2} \Omega . \quad (3)$$

Therefore, if we want to explain the observed spectrum, the product $T\Omega$ of the microwave source must be a factor 7.5 larger. In the optically thin regime, $\tau_\nu \ll 1$, Eq. 1 turns out to be:

$$F(\nu) \simeq \zeta \frac{2 k_B T \nu^2}{c^2} \frac{0.2 N_{med}^2 H}{\nu^2 T^{3/2}} \Omega$$

$$\simeq \zeta \frac{0.4 k_B}{c^2 R^2} \left(\frac{EM}{\sqrt{T}} \right), \quad (4)$$

where $EM = N_{med}^2 V$ is the emission measure, V the volume of the source and R is the Sun - Earth distance. From Eq. 4 we can infer that the product EM/\sqrt{T} must be a factor 7.5 larger; i.e. either the EM is larger or the temperature is lower, or both things are true. Therefore, considering the optically thick and optically thin regimes, we conclude that the source is neither homogeneous nor isothermal. Similar results for the gradual phase of other events were obtained by Lüthi et al. (2004) at submillimeter wavelengths, and by Chertok et al. (1995) and Sui et al. (2005) in microwaves.

5 Conclusions

In this work we have presented a multiwavelength analysis of a GOES X1 class flare, including radio data, SXR and EUV images. Radio observations cover the range between 1.4 and 405 GHz, but we have no observations between 15.4 and 212 GHz. At 212 GHz, the event has two distinct phases: impulsive and gradual. At microwave frequencies, there is a second impulsive phase whose emission at submillimeter frequencies is barely observed.

We find that the optically thin spectral index α is almost constant during the central part of the impulsive phase, afterwards there is a hardening. A transition to free-free emission, that in the optically thin regime has an almost null index, can explain the change of α .

The gradual phase observed at 212 GHz can be explained by bremsstrahlung from a thermal source. The similarity of the temporal evolution of the emission coming from an isothermal bremsstrahlung source (with EM and T deduced from SXR data) and the flux density at 212 GHz, sustains this hypothesis. Nonetheless, either the EM must be higher or T must be smaller to fit the observations. On the contrary, to fit to the microwave observations, the product $T\Omega$ must be larger. Therefore, the thermal source cannot be homogeneous.

The use of submillimeter frequencies in the analysis of burst phenomena opens new windows to understand the earlier stages of a flare at high energies, which are hard to observe with HXR detectors, and the late stages of the flare, where the thermal bremsstrahlung is normally optically thin and more intense than at microwave frequencies.

Acknowledgements. This research was partially supported by the Brazilian agency FAPESP (contract 99/06126-7) and by the Argentinean grants: UBACyT X329 (UBA), PICT 12187 (ANPCyT), PIPs 6220 and 6266 (CONICET). G.D.C. is a fellow of ANPCyT. We acknowledge the GOES/SXI team for SXI data, and the SoHO/EIT consortia for EUV data. SOHO is a project of international cooperation of ESA and NASA. The RSTN data originate at several United States Air Force monitoring stations.

References

- Chertok, I. M., Fomichev, V. V., Gorgutsa, R. V., et al., 1995. Solar Radio Bursts with a Spectral Flattening at Millimeter Wavelengths. *Sol. Phys.* 160, 181–198.
- Costa, J. E. R., Correia, E., Kaufmann, P., et al., 1995. A Method for Arc-Second Determination of Solar Burst Emission Centers with High Time Resolution and Sensitivity at 48 GHz. *Sol. Phys.* 159, 157–171.
- Daubechies, I., 1992. Ten lectures on wavelets, Society for Industrial and Applied Mathematics (SIAM). Daubechies, I. (ed).
- Delaboudiniere, J.-P., Artzner, G. E., Brunaud, J., et al., 1995. EIT: Extreme-Ultraviolet Imaging Telescope for the SOHO Mission. *Sol. Phys.* 162, 291–312.
- Dulk, G. A., 1985. Radio emission from the sun and stars. *Ann. Rev. of Ast. & Astrophys.* 23, 169–224.
- Guidice, D. A., Cliver, E. W., Barron, W. R., et al., 1981. The Air Force RSTN System. In: *Bulletin of the American Astronomical Society*. pp. 553–553.
- Hill, S. M., Pizzo, V. J., Balch, C. C., et al., 2005. The NOAA Goes-12 Solar X-Ray Imager (SXI) 1. Instrument, Operations, and Data. *Sol. Phys.* 226, 255–281.
- Kaufmann, P., Costa, J. E. R., Giménez de Castro, C. G., et al., 2001. The New Submillimeter-wave Solar Telescope. In: *Proc. of the SBMO/IEEE MTT-S International Microwave and Optoelectronics Conference*. pp. 439–441.
- Kosugi, T., Dennis, B. R., Kai, K., 1988. Energetic electrons in impulsive and extended solar flares as deduced from flux correlations between hard X-rays and microwaves. *ApJ* 324, 1118–1131.
- Lüthi, T., Lüdi, A., Magun, A., 2004. Determination of the location and effective angular size of solar flares with a 210 GHz multibeam radiometer. *A&A* 420, 361–370.
- Pizzo, V. J., Hill, S. M., Balch, C. C., Biesecker, D. A., Bornmann, P., Hildner, E., Grubb, R. N., Chipman, E. G., Davis, J. M., Wallace, K. S., Russell, K., Cauffman, S. A., Saha, T. T., Berthume, G. D., 2005. The NOAA Goes-12 Solar X-Ray Imager (SXI) 2. Performance. *Sol. Phys.* 226, 283–315.
- Sui, L., Holman, G. D., White, S. M., et al., 2005. Multiwavelength Analysis of a Solar Flare on 2002 April 15. *ApJ* 633, 1175–1186.

Torrence, C., Compo, G. P., 1998. A Practical Guide to Wavelet Analysis.
Bulletin of the American Meteorological Society 79, 61–78.